Magnetic ordering of implanted Mn in HOPG substrates

Samaresh Guchhait,[1,*,†] Hendrik Ohldag,[2,†] Elke Arenholz,[3] Domingo A. Ferrer,[1] Apurva Mehta,[2] and Sanjay K. Banerjee[1]

[1]*Microelectronics Research Center, The University of Texas at Austin, Austin, Texas 78758, USA*

[2]*Stanford Synchrotron Radiation Lightsource, Menlo Park, California 94025, USA*

[3]*Advanced Light Source, Berkeley, California 94720, USA*

(Received 12 July 2012; published 27 November 2013)

Currently, significant research efforts are geared towards using carbon-based materials for electronic applications. Here we report the observation of magnetic ordering of implanted Mn in HOPG substrates. Superconducting quantum interference device measurements show higher moments for Mn-doped samples and also the existence of double and inverted hysteresis in both undoped and doped samples. High-resolution transmission electron microscopy shows the presence of nanocrystals in implanted samples. Grazing incidence synchrotron x-ray diffraction studies show the presence of three stable manganese carbides, including antiferromagnetic $Mn_{23}C_6$. X-ray magnetic circular dichroism (XMCD) measurements show ferromagnetic ordering of Mn moments at temperatures below ∼100 K. However, a very weak XMCD signal indicates that only about 1% of Mn atoms are ferromagnetically ordered. We conclude that the observed Mn ferromagnetic ordering is caused by uncompensated Mn moments on the surface of antiferromagnetic $Mn_{23}C_6$ nanocrystals that are aligned by the local magnetic field.

DOI: 10.1103/PhysRevB.88.174425 PACS number(s): 75.50.Tt, 75.50.Ee, 78.20.Ls

I. INTRODUCTION

Magnetism is one of the oldest and most fascinating branches of physical science. Magnetic materials have diverse applications, and therefore, we are always in search of new types of magnetic materials. Over the last few years, several new types of magnetic materials have been reported. One of those is ferromagnetic graphite. This new magnetic material is particularly intriguing and also controversial because there is no element with $3d$ or $4f$ electrons. There are some reports that impurity-free highly oriented pyrolytic graphite (HOPG) shows ferromagnetism well above room temperature.[1–4] Besides HOPG, chemically synthesized graphite also shows multilevel ferromagnetism up to room temperature.[5] There is also evidence of unconventional ferromagnetism (up to 90 K) of all-carbon nanofoam prepared by laser ablation.[6] All these studies point to a new class of magnetic materials which is not fully understood yet. Recent theoretical[7–16] and experimental[3,17–22] studies point to localized moments at graphite defect sites as a possible source of magnetic moments in these all-carbon materials.

Studies on both point or local defects and line or extended defects in graphite play very important roles in understanding its magnetic properties. Density-functional theory calculations from first principles show that point defects in graphene have quasilocalized nonzero magnetic moments.[9–12] Tunneling microscopy studies performed on HOPG point-defect states agree semiquantitatively with the theoretical predictions.[17] Besides different types of point defects, there also exist two types of line defects in graphite: (zigzag and armchair) edges and grain boundaries. Isolated zigzag graphene edges are theoretically predicted to have magnetic moments due to the presence of localized edge states, and their magnetic ordering is predicted to exist only at very low temperatures.[7,13] Hydrogen-terminated graphite edges investigated by scanning tunneling microscopy (STM) indeed show the existence of a high local density of states (LDOS) at zigzag edges.[18,19] On the other hand, there exist two-dimensional (2D) arrays of interacting defect states at graphite grain boundaries. Moreover, due to local electron-electron interaction, some topological defect states at graphite grain boundaries are also spin polarized. This leads to the formation of localized magnetic moments at defect sites.[14–16] A closely packed 2D array of these strongly interacting moments at graphite grain boundaries can couple ferromagnetically with each other, and this ferromagnetic ordering can persist well above room temperature.[3] Scanning tunneling and force microscopy experiment results of HOPG grain boundaries agree quite well with these theoretical predictions.[3,20–22]

Since extended defects appear to play crucial roles in magnetic graphite, there are studies on the effects of ion implantation on graphite magnetism.[23–30] Experimental studies have shown that proton-irradiated graphite shows enhanced ferromagnetism at room temperature.[23] Soft x-ray magnetic circular dichroism (XMCD) studies performed on proton-irradiated graphite point to the spin-polarized carbon π electrons at defect states as a possible source of magnetism in these samples.[24,25] Moreover, C and N ion-implanted nanodiamond particles show ferromagnetic hysteresis behavior at room temperature.[26] Theoretical studies on ion-irradiated graphite agree well with the experimental results.[27,28] Also, using Mössbauer spectroscopy, Sielemann *et al.* have shown that implanted ^{57}Fe atoms experience a strong magnetic hyperfine field up to about 40 K.[29] All these studies have enriched our understanding of the importance of defects in graphite magnetism.

However, some studies have claimed that F, B, and Fe ions implanted into HOPG substrates have no detectable effect on its ferromagnetism.[30,31] So it seems that the magnetism of HOPG that has been manipulated via ion implantation depends strongly on the type of ion used. So far, none of these experimental studies have looked into the possible formation of binary phases of these implanted elements with carbon. Theoretical studies have predicted interesting magnetic behaviors for different implanted ions and have

TABLE I. Summary of three HOPG samples.

Sample name	Sample description	Mn-implant dose (cm^{-2})	Mn-implant energy (keV)	Peak Mn concentration (at. %)	Average Mn concentration (cm^{-3})	Magnetic moment at 5 K, 0.1 T (emu/g)
H0	Undoped HOPG			0	0	2.09×10^{-3}
H1	Mn-doped HOPG	5.5×10^{15}	20	6	3.0×10^{21}	2.17×10^{-3}
H2	Mn-doped HOPG	1.1×10^{16}	20	12	7.5×10^{21}	2.27×10^{-3}

left the conclusions ajar.[32–38] Therefore, more research is necessary to investigate these issues since all these findings will greatly influence our understanding of magnetic properties of HOPG. In this paper, we have tried to address these questions by carefully studying structural, magnetic, and polarized soft x-ray absorption properties of Mn-implanted HOPG. We have also found that both undoped and Mn-doped HOPG samples are ferromagnetic above room temperature and exhibit double and inverted hysteresis. We have also shown that implanted-Mn ions form binary phases with C. One of these binary compounds ($Mn_{23}C_6$) is antiferromagnetic with a Néel temperature of about 105 K. Nanocrystals of $Mn_{23}C_6$ have small net magnetic moments below the Néel temperature due to uncompensated moments at crystal edges. These moments align with local magnetic field below the Néel temperature and that gives rise to a very small magnetic circular dichroism effect. Field- and temperature-dependent XMCD studies show ferromagnetic ordering of Mn moments and agree well with previous hypotheses. We believe that antiferromagnetic nanocrystals embedded in HOPG could be used to study internal fields created by defects. HOPG is also a promising candidate for the combination of electronic and magnetic properties in so-called magnetoresistive devices.

II. EXPERIMENTAL DETAILS

Undoped HOPG wafers (10 mm × 10 mm × 0.2 mm) were purchased from Structure Probe, Inc. These HOPG samples are of highest quality (SPI-1 grade), which is very similar to the very best HOPG grade ZYA. The density of these HOPG wafers is 2.27 g/cm^3. Mn^+ ions were then implanted into six samples with two different doses: (a) $1.1 \times 10^{16}/cm^2$ and (b) $5.5 \times 10^{15}/cm^2$ at 20 keV energy and 7° tilt angle (three samples for each dose). The samples so obtained will be denoted as H2 and H1, respectively, and the unimplanted HOPG sample will be denoted as H0. Under these conditions, the Mn depth range is about 18 nm, the straggle is about 9 nm, and peak Mn concentration in the implanted region is about 12 and 6 at. %, respectively, as determined by TRansport of Ions in Matter (TRIM) calculations. For verification, Mn profiles of all samples were measured by time-of-flight secondary ion mass spectroscopy (TOF-SIMS). The measured averaged Mn concentration of samples H2 and H1 are $9.3 \times 10^{21}/cm^3$, and $7.5 \times 10^{21}/cm^3$, respectively (Table I). During ion implantation the samples were kept at 300 °C to minimize crystal damage. After ion implantation, the samples were cut into small pieces for synchrotron grazing-incidence x-ray diffraction (GI-XRD), XMCD, and TOF-SIMS studies, and smaller samples were taken for transmission electron microscopy (TEM) analysis. Teflon tweezers were always used throughout the experiments in order to minimize spurious ferromagnetic impurity incorporation during sample handling.

III. RESULTS AND DISCUSSION

A. Magnetic properties

In-plane magnetic moment measurements were performed down to 5 K, using a Quantum Design dc superconducting quantum interference device (dc-SQUID) magnetometer. This type of SQUID uses a plastic tube (drinking straw) to mount the sample. When the sample size is slightly larger than the plastic tube diameter, the plastic tube deforms gently and holds the sample tightly in its place. No glue was used to mount any sample. Three different sample pieces for each Mn-implant dose (H0/H1/H2) were used for magnetic measurements, and the results are very consistent within a given Mn-implant dose. Each sample mass was measured by a very sensitive scale with an accuracy of 0.1 μg, and masses of different samples range from 27 to 32 mg.

Each temperature-dependent magnetization measurement is made up of magnetic field-cooled and zero-field-cooled sweeps. However, magnetic field-cooled and zero-field-cooled plots for all three samples overlap, and no spin-glass phase is detected. As a result, only magnetic field-cooled plots for all three samples are shown here (Fig. 1). The magnetic moment measured in this setup is the sum of moments from different origins: implanted ions, defects, the Pauli paramagnetic contribution of conduction electrons, and ferromagnetism (discussed in detail later). Temperature-dependent magnetization $M(T)$

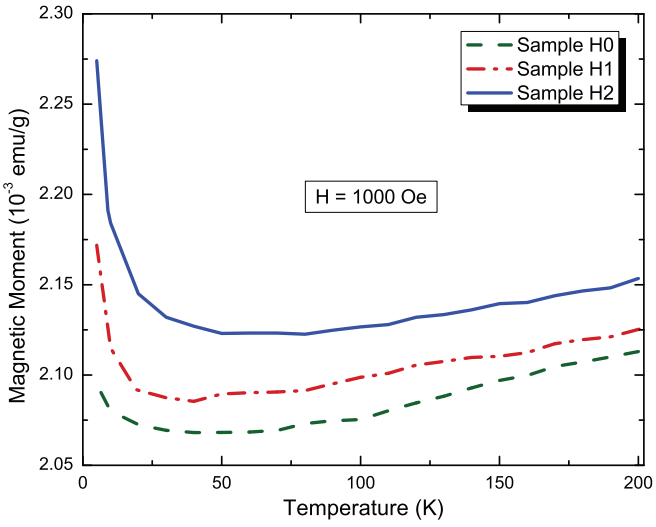

FIG. 1. (Color online) Temperature-dependent in-plane magnetic moment of three HOPG samples.

data show that the magnetic moment per unit mass is higher for both ion-implanted samples than the undoped sample. Since all three samples are mounted in an identical manner, we believe that the extra moment is coming from implanted Mn ions and defects created during ion implantation.[23] Note that the difference in magnetization observed between the three samples is significantly larger than the typical SQUID measurement error of $\sim 10^{-7}$ emu.

Although an understanding of the particular shape of the $M(T)$ curves is not critical for our study, we would like to comment on its possible origin. For Mn-implanted samples, we observe that the magnetization increases sharply below ~40 K. This might be due to the fact that more randomly oriented moments of defect sites and Mn moments are pointing along the external field below 40 K. Moreover, the magnetization of all three samples increases slowly with temperature above ~50 K, although one may expect a decrease considering the presence of ferromagnetically ordered areas of HOPG, as mentioned in the Introduction. However, these areas would be predominantly present at the surface of the material[4,25] and hence would only contribute a small magnetic moment. We therefore conclude that the observed increase is due to an increase in the Pauli paramagnetic contribution of conduction electrons in the bulk of HOPG. For metals, the Pauli paramagnetic contribution of conduction electrons is almost independent of temperature, as the temperature-dependent term is negligible at low temperatures.[39] However, theoretical[40–42] and experimental[43–45] studies have shown that graphite is a zero-band-gap semiconductor. Hence, as temperature increases, more thermally excited carriers will populate the conduction band, and hence, the Pauli paramagnetic contribution (for a fixed field) will also increase with increasing temperature.[39] This result is consistent with other studies.[2]

In-plane magnetic hysteresis measurements at different temperatures (5 to 300 K) show that both unimplanted and Mn-implanted HOPG samples are ferromagnetic at room temperature [Fig. 2(a)]. Magnetic hysteresis data also show the existence of a double and inverted hysteresis for all three samples below about 270 K. This minor inverted hysteresis is centered at about ± 6000 Oe for all three HOPG samples at 5 K [Fig. 2(b)]. As temperature increases, this minor inverted hysteresis loop also gets smaller and eventually vanishes above ~270 K. The existence of double and inverted hysteresis in HOPG has not been reported before.

Inverted magnetic hysteresis is forbidden in any magnetically homogeneous material as it violates the second law of thermodynamics. However, inverted magnetic hysteresis has been reported before in *inhomogeneous* magnetic nanostructures,[46,47] granular Co thin films,[48–50] and magnetic multilayers.[51–53] Theoretical models show that inverted magnetic hysteresis is possible in magnetically inhomogeneous materials, consisting of low- and high-coercive-field components.[47,51,54] For HOPG samples, we think there are two types of magnetic defects: one type with low coercive field (less than 100 Oe), or "soft" magnetic defects, and another type with high coercive field (about 6000 Oe or more), or "hard" magnetic defects. When the external magnetic field is positive and increasing but less than 5000 Oe, only soft magnetic defects align along the external field. Then, as applied field crosses 5000 Oe, hard defects start to align along the external field as well. However, demagnetizing and stray fields created by these hard magnetic defects could be very strong (order of tens of tesla[29]) and point opposite to the external field. At some regions near the hard defects, the net magnetic field could be opposite of the external magnetic field, and hence, soft magnetic defects will align opposite to the external field, and net magnetic moment will decrease. This process will reverse when the field is decreased from a large positive value. We think this is the origin of inverted double hysteresis in HOPG. This model is similar to the one described in Ref. 47.

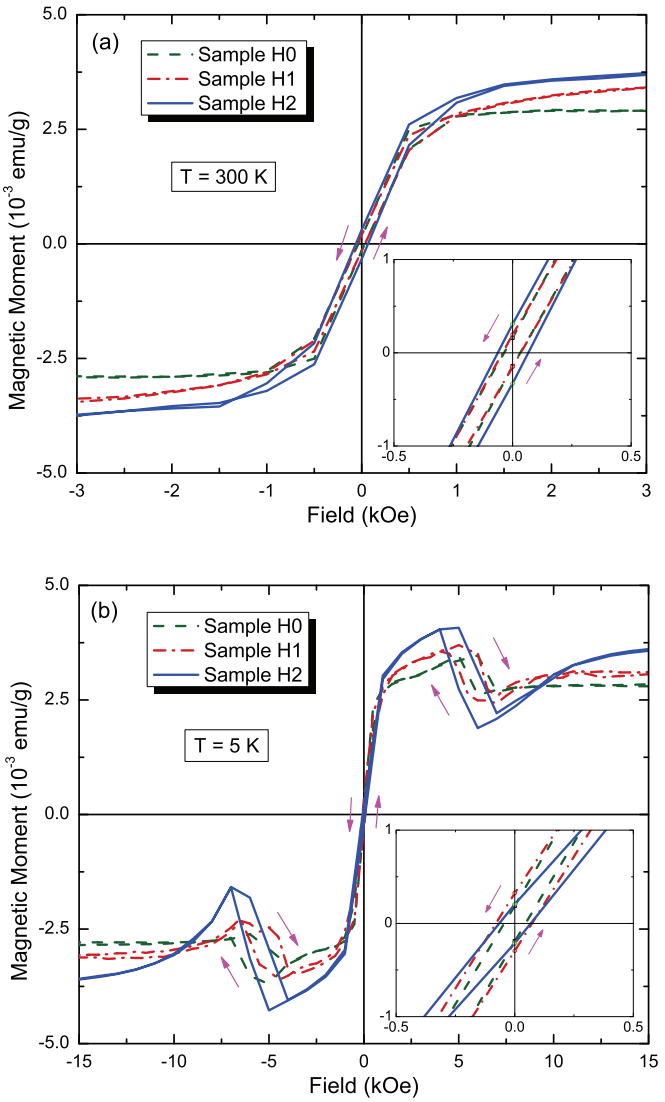

FIG. 2. (Color online) In-plane magnetic hysteresis of three HOPG samples at (a) 300 K and (b) 5 K. The insets show close-up views near the origin. The arrows show the direction of magnetic field sweep.

B. Structural characterization

In order to better understand the origin of the ferromagnetism in Mn-implanted HOPG, cross-section high-resolution transmission electron microscopy (HR-TEM) and GI-XRD were performed on the samples. A FEI Altura 835 focused ion beam (FIB) system with a 30-keV Ga^+ beam and final 50-pA

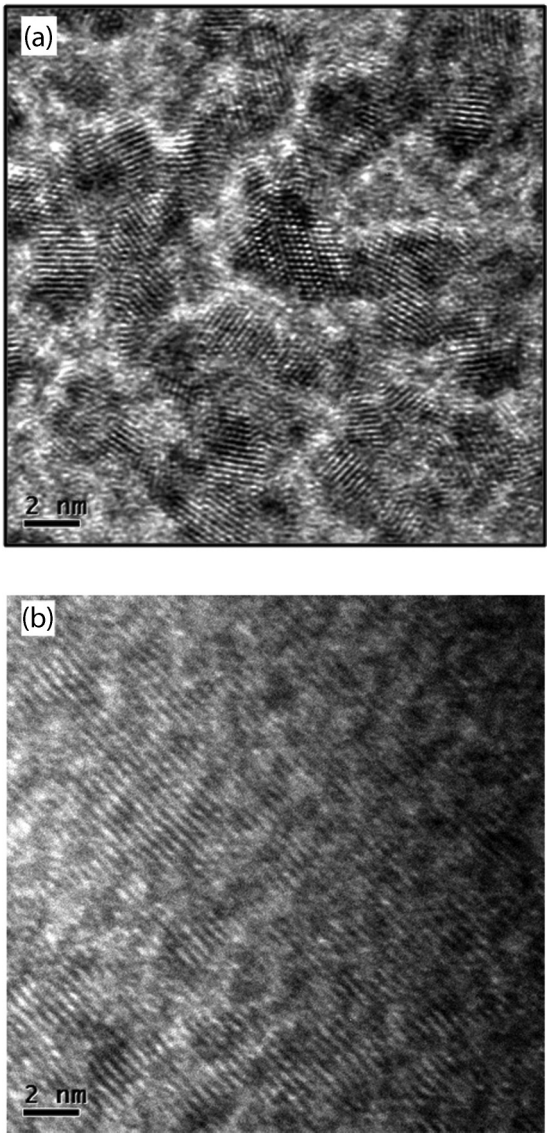

FIG. 3. High-resolution cross-section TEM images of (a) sample H2 and (b) unimplanted HOPG.

current was used to prepare an electron-transparent lamella for TEM inspection. The HR-TEM image of the Mn ion-implanted HOPG sample shows the presence of a nanocrystal-embedded amorphous implanted region [Fig. 3(a)]. The HR-TEM image also reveals that these nanocrystals are around 4–8 nm in diameter and randomly oriented. In comparison, the HR-TEM image of the unimplanted HOPG sample shows only stacked layers of graphite sheets [Fig. 3(b)].

In order to understand the compositions of these nanocrystals, we performed synchrotron GI-XRD studies of Mn ion-implanted HOPG sample at beam line 11-3 of Stanford Synchrotron Radiation Lightsource (SSRL). This beam line has a large-area detector of 345-mm diameter and 60–90-s read-out time. The beam line x-ray energy is 12735 eV, and spot size is about 3 mm by 0.15 mm. This large-area detector is very useful for acquiring the x-ray diffraction pattern from low-density randomly oriented nanocrystals embedded in a crystalline or amorphous matrix. Regular x-ray diffraction patterns (2θ vs. intensity) are extracted from these images

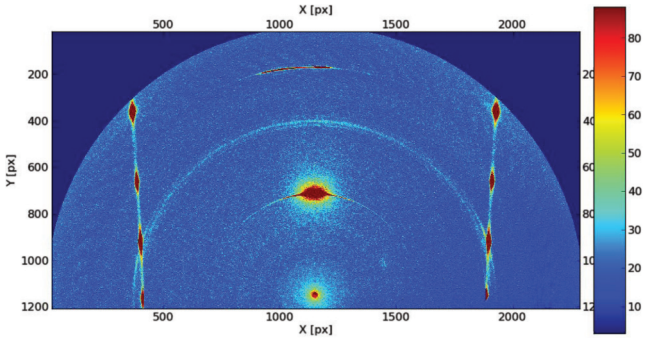

FIG. 4. (Color online) Large area detector synchrotron x-ray diffraction image of sample H2 at an incidence angle of 0.9°.

by diffraction image processing and the data analysis software WXDIFF, which was developed by SSRL.

Figure 4 shows the x-ray diffraction image of the H2 sample obtained by a large-area detector at beam line 11-3 of SSRL. The image consists of many strong peaks (red spots in the image) and few semicircular diffraction patterns (light blue rings). The peak at the bottom center is where the x-ray beam line hits the detector plate. All strong peaks, including those aligned along the two straight lines, are diffraction patterns from the highly oriented substrate. Semicircular diffraction lines are a signature of the powder diffraction pattern from nanocrystalline samples. These images are converted into traditional XRD patterns (Fig. 5) by WXDIFF and then analyzed.

GI-XRD patterns of the Mn-implanted HOPG sample are collected at three grazing incidence angles of 0.1°, 0.5°, and 0.9°. For those incidence angles and 12735 eV of photon energy, the x-ray penetration depths for $C_{0.84}Mn_{0.16}$ are about 5 nm, 1 μm, and 2 μm, respectively. All XRD patterns clearly show the presence of very strong (002) and (004) peaks of graphite substrate. Besides these two sharp substrate peaks, higher-incidence-angle GI-XRD data clearly show the presence of six broader, and relatively weaker, distinct peaks which match with (102) Mn_7C_3; (211), (120), (213), and (115) Mn_5C_2; and (531) $Mn_{23}C_6$ peaks. Around a diffraction

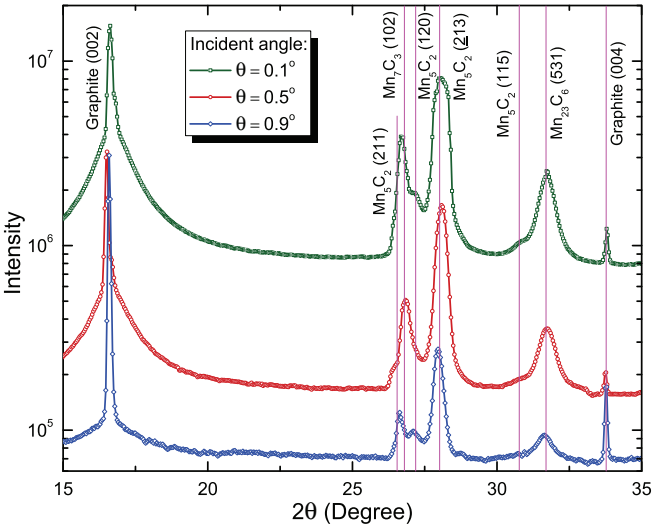

FIG. 5. (Color online) Grazing-angle synchrotron x-ray diffraction pattern of sample H2.

angle of 26.6°, there are two closely spaced peaks, which fit well with the (102) Mn_7C_3 and (211) Mn_5C_2 peaks. Since the semicircular lines of the x-ray diffraction image (Fig. 4) give rise to these six XRD peaks (Fig. 5), we conclude that these peaks come from randomly oriented nanocrystals of three stable manganese carbides embedded in the ion-implanted HOPG matrix. Moreover, the (531) $Mn_{23}C_6$ diffraction peak at 31.5° is very broad (Fig. 5) and has a full width at half maxima (FWHM) of ∼0.5°. This gives an average size of $Mn_{23}C_6$ nanocrystals of ∼5 nm. A similar exercise with other peaks gives an average size of ∼4–7 nm of other nanocrystals. This agrees well with the HR-TEM image of nanoparticles (Fig. 3). It is also important to note that there is no distinguished surface oxide peak in the XRD data.

The Mn-C binary system has a very complex phase diagram.[55] Structural and thermodynamic properties of C and Mn binary compound phases have been studied for a long time,[55–61] and as many as 12 compound phases are predicted to exist. However, only three phases ($Mn_{23}C_6$, Mn_5C_2, and Mn_7C_3) are claimed to be thermodynamically stable at room temperature, and these phases are also studied extensively.[56,57] While Mn_5C_2 and Mn_7C_3 are known to be paramagnetic (measured down to 16 K), $Mn_{23}C_6$ is antiferromagnetic (AFM), with a Néel temperature of about 108 ± 5 K.[57] Crystal-structure studies of these three compounds show that the average Mn-Mn distances increase in this sequence: $Mn_{23}C_6 < Mn_5C_2 < Mn_7C_3$. Hence, we can assume that the average Mn-Mn bond strengths decrease in this sequence: $Mn_{23}C_6 > Mn_5C_2 > Mn_7C_3$.[57] That might well explain the existence of magnetic ordering in $Mn_{23}C_6$ but not in Mn_5C_2 or Mn_7C_3. The irregular shape and few nanometer-size crystals of the AFM $Mn_{23}C_6$ compound will have uncompensated moments at crystal edges, and hence, these nanocrystals will have a small, but *nonzero*, magnetic moment below the Néel temperature. These magnetic moments will line up along the local magnetic field within the HOPG substrate. Therefore, studying the magnetic ordering of AFM $Mn_{23}C_6$ nanocrystals will tell us about local magnetic field at the nanometer scale within the HOPG substrate.

C. Synchrotron soft x-ray absorption studies

Soft x-ray absorption spectroscopy and circular dichroism measurements were taken at beam line 6.3.1 at the Advanced Light Source in Berkeley.[62] This facility employs circular x-rays, generated by synchrotron bending magnets, for XMCD spectroscopy. XMCD spectroscopy is capable of obtaining element-specific information for each elemental species in a complex sample.[63] For this purpose one scans the energy of the incoming x-ray photons across a core level resonance, in our case the Mn $2p-3d$ transition, and monitors the absorbed x-ray intensity. For very thin samples (<1 mm) one can directly measure the intensity transmitted through the sample. For thick samples, however, one may choose to detect the intensity of photoelectrons and secondary electrons from the sample. The electron yield is directly proportional to the x-ray absorption cross section of the sample surface. The total probing depth is typically about 10–15 nm.[64] When using circular polarization, this approach becomes sensitive to the spin polarization of the $3d$ final states, and the resonant absorption intensity will show

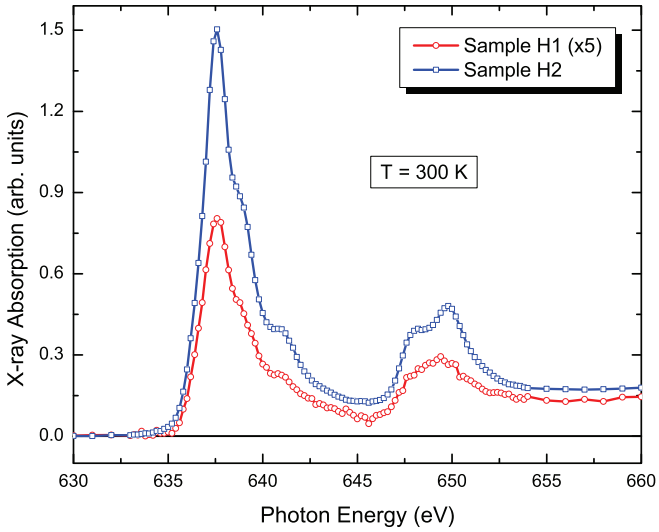

FIG. 6. (Color online) X-ray absorption spectra of two Mn-doped HOPG samples.

strong differences, several tens of percent, depending on the relative orientation of the magnetization of the sample and the direction of the incoming x-rays. Altogether, element-specific information about the total magnetic moment for each element in the sample as well as its chemical configuration can be obtained.

To address the chemical state of the Mn sites, we first acquired x-ray absorption spectra (XAS) using the electron-yield-detection approach. The result is shown in Fig. 6. The spectra of samples H1 and H2 are qualitatively identical, showing identical spectral features, considering that the signal-to-noise ratio is reduced for sample H1. Note that the spectrum of sample H1 has been multiplied by a factor of 5 for easier comparison. As pointed out above, the Mn atoms are implanted to a depth of about 18 nm with a straggle of 9 nm, which is at the limit of our exponential probing depth of 10–15 nm. For this reason the Mn concentration in sample H1 was too low for subsequent magnetic XMCD measurements. However, since the presence of oxygen at the surface of the HOPG did not affect the Mn sites, as discussed in the following, we can assume that our x-ray setup probes a representative subset of the sample.

We now compare the observed spectral shape to previously published x-ray absorption studies on Mn-implanted samples.[65,66] In general, we find that the spectrum is typical for Mn^{2+} atoms in spherical coordination symmetry. However, the spectra of samples H1 and, in particular, H2 are missing the strong multiplet features that are characteristic for Mn-rich surface oxide phases observed in early $Ga_{1-x}Mn_xAs$ measurements.[67] This indicates that the majority of the Mn atoms are indeed implanted in deeper layers of the HOPG and that Mn oxidation does not play a significant role in our samples, which also agrees well with GI-XRD data (Fig. 5). The x-ray absorption spectra obtained from our sample in this study exhibit a very similar line shape with smooth multiplets, as reported by Stone *et al.* on $Ga_{1-x}Mn_xP$.[66] Since the shape of the L-edge XAS of the $3d$ transition metals is a direct measure of the density of states above the Fermi level and the coordination of the elemental species, we can

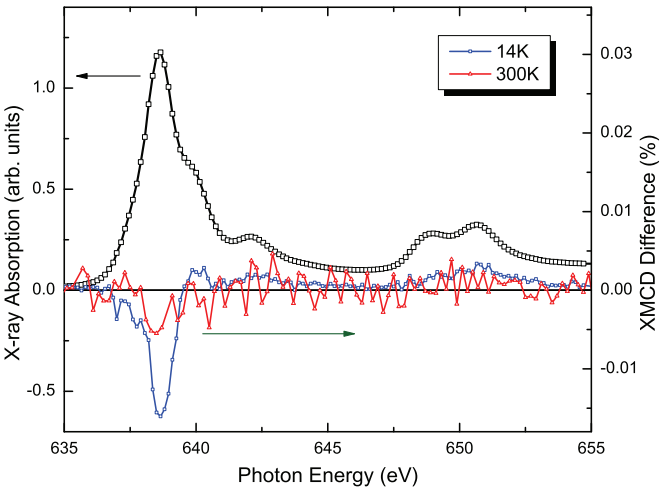

FIG. 7. (Color online) Manganese x-ray absorption spectra (at 14 K) and XMCD at 14 and 300 K of sample H2.

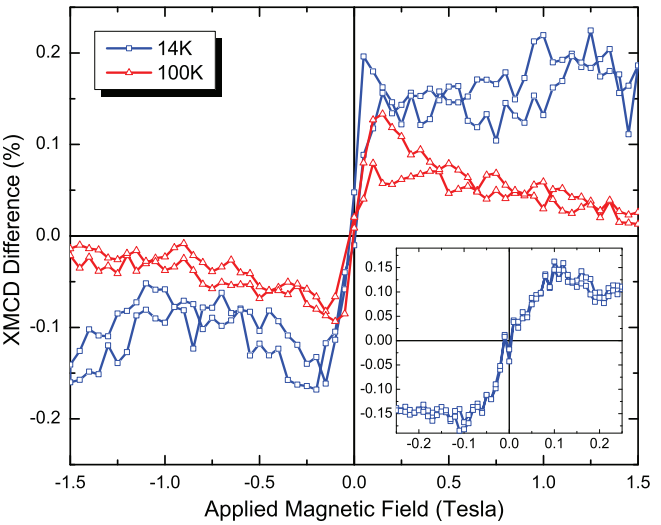

FIG. 8. (Color online) Manganese XMCD major loop hysteresis of sample H2. The inset shows minor loop hysteresis at 14 K.

conclude that the Mn atoms in our samples are in a chemical environment similar to the Mn atoms in Ref. 66 characterized by d orbitals hybridized with p orbitals of neighboring atoms in the matrix with spherical symmetry. Even more important, we can conclude that the magnetic moment per d shell is similar to the one found in Ref. 66, which is $\sim 3\mu_B$.

In the following section, we focus on the magnetic properties of sample H2 since this signal showed the most favorable signal-to-noise ratio. For this purpose we measured XMCD spectra by applying ± 1.0 tesla along the x-ray beam direction and subtracting the resulting spectra from each other. The results obtained for sample H2 at 14 K and room temperature are shown in Fig. 7. At 14 K we observe an XMCD spectrum that shows all features that are expected for Mn in this configuration, as we reported earlier in our studies on Ge:Mn (Ref. 65) and as has been observed by Stone *et al.*[66] However, the magnitude of the XMCD signal is much smaller than expected for Mn, with a magnetic moment of about $3\mu_B$. In our case we observe an XMCD of about 0.7% at the Mn L_3 resonance edge (638.7 eV), although an XMCD of up to 70% has been reported previously.[66] Since the XMCD effect is directly proportional to the atomic magnetic moment aligned with the external field, we can conclude that only about 1% of the Mn atoms in our sample order ferromagnetically, while the remaining Mn atoms are located in antiferromagnetically ordered and/or paramagnetic sites. Note that XMCD spectra obtained at room temperature shown in Fig. 7 exhibit faint evidence for residual magnetic order at room temperature.

To address the question of whether the small XMCD signal observed by us is indeed caused by ferromagnetic order and not simply by the paramagnetic response of our sample, we acquired element-specific hysteresis loops of sample H2 by scanning the external field while tuning the energy of the incoming x-rays to the maximum of the XMCD signal at the L_3 and the L_2 resonances. The normalized difference between these two scans is plotted in Fig. 8. We show minor and major hysteresis loops for comparison. While this normalization approach is quite effective and allows for detection of a very small XMCD difference down to 0.05%, some signal drifts remain, as evident from the plot. Nevertheless, the hysteresis loops observed with x-rays reproduce the ones observed with SQUID [as shown in Fig. 2(b)] very well, indicating that the macroscopically observed magnetic hysteresis is indeed caused by magnetically ordered Mn atoms. However, the element-specific loops show no evidence of the inverted hysteresis at higher fields that the macroscopic SQUID loops show. This is direct proof of our earlier assumption that the inverted hysteresis is caused by the presence of soft and hard magnetic defects in the HOPG matrix and not by the implanted-Mn sites.

Finally, we present the results of the temperature-dependent XMCD studies of sample H2 (Fig. 9). For this experiment we varied the sample temperature between 15 K and room temperature and measured the x-ray absorption spectra and x-ray magnetic circular dichroism at the L_3 resonance edge. To compare spectra obtained at different temperatures quantitatively we shifted the preedge intensity in the x-ray absorption spectra to zero and scaled the L_3 intensity to 1, before

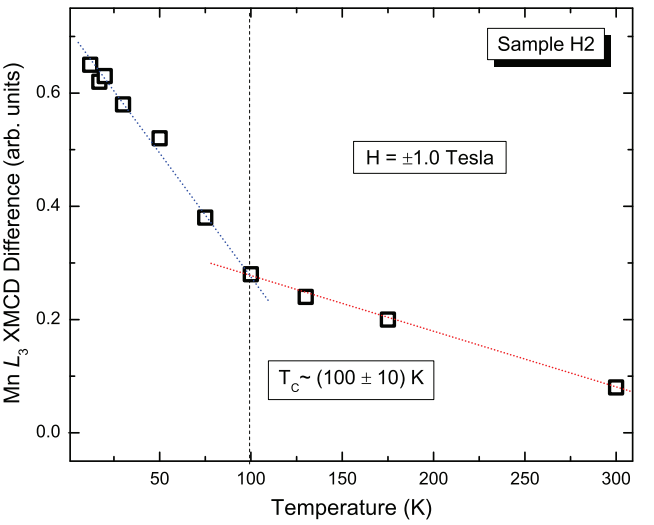

FIG. 9. (Color online) Temperature dependence of manganese XMCD.

calculating the XMCD difference. Upon warming up the sample, the XMCD intensity drops continuously at a constant rate until about 100 ± 10 K. However, the XMCD intensity does not vanish completely above 100 K, but the rate at which it decreases is reduced significantly. Our interpretation of this behavior is that below ∼100 K, uncompensated moments of AFM $Mn_{23}C_6$ nanocrystals align themselves along their local magnetic field, and we think that is the origin of steep increase of XMCD below that temperature. Above ∼100 K, some remaining fraction of the Mn sites is magnetically polarized through the HOPG matrix. Note that it has been previously reported that HOPG can exhibit ferromagnetic order well above room temperature.[1–4,24,25] As a consequence, a net XMCD can be observed in our samples even at room temperature.

D. Possible applications

Defect-induced ferromagnetism in HOPG is very fascinating and may be useful too, but it is very difficult to engineer structural defects. On the other hand, controlled ion irradiation could be a great way to harness magnetic graphite. Ferromagnetism at room temperature opens up the possibility of novel spintronic applications. One can envision patterned Mn-implanted graphite quantum dots that can be the basis of magnetic quantum-dot cellular automata (MQCA).[68] Since graphene has been reported to have long spin diffusion lengths,[69] it may be possible to have all spin logic[70] based on ion-implanted graphite ferromagnets coupled with graphene interconnects. Here, the magnetic quantum dots would be flipped not by dipolar coupling as in MQCA, but by spin-polarized electrons.

IV. SUMMARY AND CONCLUSION

Our studies show that both undoped and Mn-doped HOPG exhibit ferromagnetism well above room temperature. They also display the existence of double and inverted hysteresis in both undoped and doped samples, indicating the presence of defects with different coercive fields. The HR-TEM image shows few nanometer diameter crystals embedded in the HOPG substrate. Synchrotron GI-XRD shows the formation of three stable manganese carbides in doped samples. One of the binary compounds ($Mn_{23}C_6$) is antiferromagnetic, with a Néel temperature of about 105 K. Nanocrystals of this AFM phase will have uncompensated moments at the crystal edges, and hence, each nanocrystal will have a nonzero magnetic moment below the Néel temperature.

Altogether our x-ray measurements show that the Mn atoms implanted in our samples are indeed implanted in deeper layers, and we do not observe a signature of significant oxidation. The x-ray absorption line shape indicates an average magnetic moment of about $3\mu_B$ per Mn atom. However, in a magnetic field of 1.5 tesla, we find that only a few percent of Mn moments can be aligned with the external field, indicating that different magnetic phases of Mn are present, including antiferromagnetic phases. Element-specific hysteresis loops showed that the net magnetic moment observed by XMCD is due to ferromagnetic ordering and not due to paramagnetic response. No evidence for inverted hysteresis has been observed in the Mn loops, indicating that the macroscopically observed inverted hysteresis is a property of the host HOPG. The ordering temperature of the ferromagnetic Mn phase is around 100 K. Hence, we conclude that uncompensated moments of AFM $Mn_{23}C_6$ nanocrystals are ferromagnetically ordered. The ferromagnetic XMCD response observed up to room temperature is caused by magnetic polarization of Mn by the host HOPG substrate.

ACKNOWLEDGMENTS

This work is supported by SWAN-NRI, NSF NNIN, NSF ERC-NASCENT, NSF DMR Grant No. 0605828, and Welch Foundation Grant No. F-1191. SSRL and ALS are national user facilities supported by the Department of Energy, Office of Basic Energy Sciences. SSRL is operated by Stanford University. ALS is operated by the University of California under Contract No. DE-AC02-05CH11231.

*samaresh@physics.utexas.edu

†Both of these authors contributed equally to this paper.

[1] P. Esquinazi, A. Setzer, R. Höhne, C. Semmelhack, Y. Kopelevich, D. Spemann, T. Butz, B. Kohlstrunk, and M. Lösche, Phys. Rev. B **66**, 024429 (2002).

[2] P. Esquinazi and R. Höhne, J. Magn. Magn. Mater. **290–291**, 20 (2005).

[3] J. Červenka, M. I. Katsnelson, and C. F. J. Flipse, Nat. Phys. **5**, 840 (2009).

[4] P. Esquinazi, J. Barzola-Quiquia, D. Spemann, M. Rothermel, H. Ohldag, N. Garcia, A. Setzer, and T. Butz, J. Magn. Magn. Mater. **322**, 1156 (2010).

[5] A. W. Mombrú, H. Pardo, R. Faccio, O. F. de Lima, E. R. Leite, G. Zanelatto, A. J. C. Lanfredi, C. A. Cardoso, and F. M. Araújo-Moreira, Phys. Rev. B **71**, 100404(R) (2005).

[6] A. V. Rode, E. G. Gamaly, A. G. Christy, J. G. Fitz Gerald, S. T. Hyde, R. G. Elliman, B. Luther-Davies, A. I. Veinger, J. Androulakis, and J. Giapintzakis, Phys. Rev. B **70**, 054407 (2004).

[7] M. Fujita, K. Wakabayashi, K. Nakada, and K. Kusakabe, J. Phys. Soc. Jpn. **65**, 1920 (1996).

[8] N. Park, M. Yoon, S. Berber, J. Ihm, E. Osawa, and D. Tománek, Phys. Rev. Lett. **91**, 237204 (2003).

[9] M. A. H. Vozmediano, M. P. López-Sancho, T. Stauber, and F. Guinea, Phys. Rev. B **72**, 155121 (2005).

[10] N. M. R. Peres, F. Guinea, and A. H. Castro Neto, Phys. Rev. B **73**, 125411 (2006).

[11] O. V. Yazyev and L. Helm, Phys. Rev. B **75**, 125408 (2007).

[12] T. O. Wehling, A. V. Balatsky, M. I. Katsnelson, A. I. Lichtenstein, K. Scharnberg, and R. Wiesendanger, Phys. Rev. B **75**, 125425 (2007).

[13] O. V. Yazyev and M. I. Katsnelson, Phys. Rev. Lett. **100**, 047209 (2008).

[14] S. Malola, H. Häkkinen, and P. Koskinen, Phys. Rev. B **81**, 165447 (2010).

[15] O. V. Yazyev and S. G. Louie, Phys. Rev. B **81**, 195420 (2010).

[16] A. Mesaros, S. Papanikolaou, C. F. J. Flipse, D. Sadri, and J. Zaanen, Phys. Rev. B **82**, 205119 (2010).
[17] Y. Niimi, H. Kambara, T. Matsui, D. Yoshioka, and H. Fukuyama, Phys. Rev. Lett. **97**, 236804 (2006).
[18] Y. Kobayashi, K. I. Fukui, T. Enoki, K. Kusakabe, and Y. Kaburagi, Phys. Rev. B **71**, 193406 (2005).
[19] Y. Kobayashi, K. I. Fukui, T. Enoki, and K. Kusakabe, Phys. Rev. B **73**, 125415 (2006).
[20] H. Wang, A. C. Papageorgopoulosa, and N. Garcia, Eur. Phys. J. B **40**, 499 (2004).
[21] Y. Lu, M. Muñoz, C. S. Steplecaru, C. Hao, M. Bai, N. Garcia, K. Schindler, and P. Esquinazi, Phys. Rev. Lett. **97**, 076805 (2006).
[22] J. Červenka and C. F. J. Flipse, Phys. Rev. B **79**, 195429 (2009).
[23] P. Esquinazi, D. Spemann, R. Höhne, A. Setzer, K.-H. Han, and T. Butz, Phys. Rev. Lett. **91**, 227201 (2003).
[24] H. Ohldag, T. Tyliszczak, R. Höhne, D. Spemann, P. Esquinazi, M. Ungureanu, and T. Butz, Phys. Rev. Lett. **98**, 187204 (2007).
[25] H. Ohldag, P. Esquinazi, E. Arenholz, D. Spemann, M. Rothermel, A. Setzer, and T. Butz, New J. Phys. **12**, 123012 (2010).
[26] S. Talapatra, P. G. Ganesan, T. Kim, R. Vajtai, M. Huang, M. Shima, G. Ramanath, D. Srivastava, S. C. Deevi, and P. M. Ajayan, Phys. Rev. Lett. **95**, 097201 (2005).
[27] P. O. Lehtinen, A. S. Foster, Y. Ma, A. V. Krasheninnikov, and R. M. Nieminen, Phys. Rev. Lett. **93**, 187202 (2004).
[28] O. V. Yazyev, Phys. Rev. Lett. **101**, 037203 (2008).
[29] R. Sielemann, Y. Kobayashi, Y. Yoshida, H. P. Gunnlaugsson, and G. Weyer, Phys. Rev. Lett. **101**, 137206 (2008).
[30] R. Höhne, P. Esquinazi, V. Heera, H. Weishart, A. Setzer, and D. Spemann, J. Magn. Magn. Mater. **320**, 966 (2008).
[31] J. Barzola-Quiquia, R. Höhne, M. Rothermel, A. Setzer, P. Esquinazi, and V. Heera, Eur. Phys. J. B **61**, 127 (2008).
[32] A. V. Krasheninnikov, P. O. Lehtinen, A. S. Foster, P. Pyykkö, and R. M. Nieminen, Phys. Rev. Lett. **102**, 126807 (2009).
[33] V. K. Dugaev, V. I. Litvinov, and J. Barnas, Phys. Rev. B **74**, 224438 (2006).
[34] M. Daghofer, N. Zheng, and A. Moreo, Phys. Rev. B **82**, 121405(R) (2010).
[35] F. M. Hu, T. Ma, H.-Q. Lin, and J. E. Gubernatis, Phys. Rev. B **84**, 075414 (2011).
[36] H. Lee, Y.-W. Son, N. Park, S. Han, and J. Yu, Phys. Rev. B **72**, 174431 (2005).
[37] M. Inglot and V. K. Dugaev, J. Phys. Conf. Ser. **213**, 012032 (2010).
[38] D. W. Boukhvalov, Phys. Status Solidi B **248**, 1347 (2011).
[39] N. W. Ashcroft and N. D. Mermin, *Solid State Physics* (Cengage Learning, Toebben Drive, Independence, KY, 1976).
[40] J. C. Slonczewski and P. R. Weiss, Phys. Rev. **109**, 272 (1958).
[41] R. C. Tatar and S. Rabii, Phys. Rev. B **25**, 4126 (1982).
[42] J.-C. Charlier, J.-P. Michenaud, X. Gonze, and J.-P. Vigneron, Phys. Rev. B **44**, 13237 (1991).
[43] T. Takahashi, H. Tokailin, and T. Sagawa, Phys. Rev. B **32**, 8317 (1985).
[44] I. Schäfer, M. Schlüter, and M. Skibowski, Phys. Rev. B **35**, 7663 (1987).
[45] F. Maeda, T. Takahashi, H. Ohsawa, S. Suzuki, and H. Suematsu, Phys. Rev. B **37**, 4482 (1988).
[46] X. Yan and Y. Xu, J. Appl. Phys. **79**, 6013 (1996).
[47] J. Y. Yang, J. H. Kim, J. S. Lee, S. J. Woo, J. S. Kwak, J. P. Hong, and M. H. Jung, Phys. Rev. B **78**, 094415 (2008).
[48] J. Geshev, A. D. C. Viegas, and J. E. Schmidt, J. Magn. Magn. Mater. **196–197**, 126 (1999).
[49] M. F. Chioncel, P. W. Haycock, F. Y. Ogrin, B. L. Ruthven, and J. W. Bull, Mater. Res. Soc. Symp. Proc. **616**, 3 (2000).
[50] P. W. Haycock, M. F. Chioncel, and J. Shah, J. Magn. Magn. Mater. **242–245**, 1057 (2002).
[51] P. Poulopoulos, R. Krishnan, and N. K. Flevaris, J. Magn. Magn. Mater. **163**, 27 (1996).
[52] W. Van Roy, H. Akinaga, S. Miyanishi, K. Tanaka, and L. H. Kuo, J. Magn. Magn. Mater. **165**, 149 (1997).
[53] L. M. Alvarez-Prado, F. H. Salas, and J. M. Alameda, J. Magn. Magn. Mater. **196–197**, 796 (1999).
[54] A. Aharoni, J. Appl. Phys. **76**, 6977 (1994).
[55] A. Tanaka, Trans. Jpn. Inst. Met. **20**, 516 (1979), http://www.jim.or.jp/journal/e/20/09/516.html.
[56] F. Moattar and J. S. Anderson, Trans. Faraday Soc. **67**, 2303 (1971).
[57] P. Karen, H. Fjellvåg, A. Kjekshus, and A. F. Andresen, Acta Chem. Scand. **45**, 549 (1991).
[58] A. Aouni and E. Bauer-Grosse, J. Phys. IV France **3**, C7-2189 (1993).
[59] A. Aouni and E. Bauer-Grosse, J. Alloys Compd. **335**, 157 (2002).
[60] A. I. Zaitsev, N. E. Zaitseva, Yu. P. Alekseeva, and S. F. Dunaev, Dokl. Phys. Chem. **395**, 94 (2004).
[61] E. Bauer-Grosse, Thin Solid Films **447–448**, 311 (2004).
[62] P. Nachimuthu, J. H. Underwood, C. D. Kemp, E. M. Gullikson, D. W. Lindle, D. K. Shuh, and R. C. C. Perera, in *Synchrotron Radiation Instrumentation: Eighth International Conference on Synchrotron Radiation Instrumentation*, AIP Conf. Proc. No. 705 (AIP, New York, 2004), p. 454.
[63] J. Stöhr and H. C. Siegmann, *Magnetism, from Fundamentals to Nanoscale Dynamics* (Springer, Berlin, 2006).
[64] J. Stöhr, *NEXAFS Spectroscopy* (Springer, Berlin, 1992).
[65] S. Guchhait, M. Jamil, H. Ohldag, A. Mehta, E. Arenholz, G. Lian, A. Li-Fatou, D. A. Ferrer, J. T. Markert, L. Colombo, and S. K. Banerjee, Phys. Rev. B **84**, 024432 (2011).
[66] P. R. Stone, M. A. Scarpulla, R. Farshchi, I. D. Sharp, E. E. Haller, O. D. Dubon, K. M. Yu, J. W. Beeman, E. Arenholz, J. D. Denlinger, and H. Ohldag, Appl. Phys. Lett. **89**, 012504 (2006).
[67] H. Ohldag, V. Solinus, F. U. Hillebrecht, J. B. Goedkoop, M. Finazzi, F. Matsukura, and H. Ohno, Appl. Phys. Lett. **76**, 2928 (2000).
[68] A. Orlov, A. Imre, G. Csaba, L. Ji, W. Porod, and G. H. Bernstein, J. Nanoelectron. Optoelectron. **3**, 55 (2008).
[69] N. Tombros, C. Jozsa, M. Popinciuc, H. T. Jonkman, and B. J. van Wees, Nature (London) **448**, 571 (2007).
[70] B. Behin-Aein, D. Datta, S. Salahuddin, and S. Datta, Nat. Nanotechnol. **5**, 266 (2010).